INT. J. NUM. METH. HEAT FLUID FLOW, VOL. 5, 629–645 (1995)

A NUMERICAL STUDY OF TRANSIENT NATURAL CONVECTION ABOUT A CORRUGATED PLATE EMBEDDED IN AN ENCLOSED POROUS MEDIUM

SHIH-WEN HSIAO

Department of Industrial Design, National Cheng-Kung University, Tainan, Taiwan 70101, R.O.C.

ABSTRACT

The problems of transient natural convection from a corrugated plate embedded in an enclosed porous medium is studied numerically. The non-Darcian effects as well as the acceleration terms are taken into consideration in the momentum equation. The governing equations in terms of vorticity, stream function and temperature are expressed in a body-fitted coordinates system, which were solved numerically by the finite difference method. Results are presented in terms of streamlines and isotherms, local and average Nusselt numbers, with Darcy-Rayleigh number ranging from 0 to 1000, and Darcy number from 10^{-4} to 10^{-1}, for several aspect ratios of the cavity and plate positions. The flow and heat transfer characteristics for a corrugated plate and a flat plate and the numerical results solved with four different mathematical models are also compared.

KEY WORDS Natural convection Corrugated plate Porous medium Body-fitted Finite difference

INTRODUCTION

A great deal of attention has been given to the study of natural convection in enclosures filled with a porous medium due to its widespread engineering applications, including geothermal systems, underground spread of pollutants, heat exchangers, storage of nuclear waste materials, solification of castings and thermal insulation and electronic cooling. In all these areas, both experimental and theoretical works have been undertaken to determine the influence of important parameters such as Darcy number, Rayleigh number, Prandtl number, cavity aspect ratio and conductivity ratio between solid and fluid phases.

Most of the early studies were based on Darcy's law with the assumptions of a constant porosity medium[1–3]. But, Tong *et al.*[4] studied the problem of natural convection in vertical porous enclosures, based on Darcy's law and boundary layer approximations, and found that pure Darcy analysis is applicable only when $RaDa^2/A < O(10^{-4})$. Beckermann *et al.*[5,6] studied the inertia and viscous effects by using the Brinkman–Forchheimer-extended Darcy equations, and found that at high Darcy numbers the inertia and viscous terms must be included simultaneously to obtain realistic predictions of the Nusselt number. Georgiadis and Catton[7] also used Brinkman's and Forchheimer's extensions of Darcy's law to study non-Darcian free convective motion in an infinite vertical porous slot and found that both effects are important at high Darcy numbers.

Experimental investigations on natural convection in a confined rectangular cavity packed with porous medium, were carried out by Seki *et al.*[8] as well as Jonsson *et al.*[9]. It has been concluded that the Nusselt number no longer increases with increasing Prandtl number and it

0961–5539/95/070629–17$2.00

Received August 1993
Revised May 1994

NOMENCLATURE

A	aspect ratio of the cavity, W/H
B	constant defined in (21)
C	Forchheimer coefficient
C_1	distance between the flat surface and the valley of the corrugation, $=\frac{1}{2}C_2$
C_2	thickness of the plate
C_p	specific heat at constant pressure
D	constant defined in (21)
Da	Darcy number, K/H_2^2
E	consant defined in (21)
F	function defined in (15,) and (16)
f	quantity defined in (28)
g	gravitational acceleration
H	height of cavity
H_1	distance between the top of the heated plate and the top of the cavity
H_2	length of plate
H_3	distance between the bottom of the heated plate and the bottom of the cavity
J	Jacobian of the coordinate transformation defined in (19)
k	thermal conductivity
K	permeability
m	number of iteration
n	normal direction
$\underline{Nu}$	local Nusselt number defined in (29)
Nu	mean Nusselt number defined in (30)
Pr	Prandtl number of a saturated porous medium
p^*	dimensional pressure
P, Q	coordinate control functions
R	radius ratio for a concentric porous annulus
Ra	Rayleigh number, $g\beta_f(T_h^*-T_c^*)H_2^3/\nu\alpha_e$
Ra_m	Darcy–Rayleigh number, $g\beta_f KH_2(T_h^*-T_c^*)/\nu\alpha_e$
T^*, T	dimensional and dimensionless temperature defined in (5)
t^*, t	dimensional and dimensionless time defined in (5)
u^*, u	dimensional and dimensionless Darcian velocities in the x-direction defined in (5)
v^*, v	dimensional and dimensionless Darcian velocities in the y-direction defined in (5)
w^*, w	dimensional and dimensionless absolute velocities
x^*, x	dimensional and dimensionless coordinates in the horizontal direction defined in (5)
y^*, y	dimensional and dimensionless coordinates in the vertical direction defined in (5)

Greek symbols

α, β, γ	transformation factors given in (19)
α_e	effective thermal diffusivity, $k_e/\rho_f C_{pf}$
β_f	thermal expension coefficient
μ	dynamic viscosity
ν	kinematic viscosity
ρ	density
ε	porosity
θ	corrugated angle
ξ, η	dimensionless transformed coordinates
σ	heat capacity ratio
Ψ	dimensionless stream function defined in (9)
Ω	dimensionless vorticity defined in (9)
ψ, ϕ	functions defined in (20)
∇^2	Laplace operator in the (x,y) coordinates
$\tilde{\nabla}^2$	Laplace operator in the transformed coordinates

can be assumed to be infinite as the effective Prandtl number becomes greater than 0.1. The problem of natural convective heat transfer across a vertical impermeable partition imbedded in porous medium has been studied by Bejan *et al.* [10]. Another numerical investigation of the effect of internal flow obstructions on heat transfer through a 2-D porous layer heated from the side has been performed by Bejan[11]. It was found that a vertical diathermal partition reduces, by about 50%, the heat transfer rate in a convection dominated porous layer and the effect of horizontal partitions depends on the heat transfer mechanism.

The problem of heat losses from buried pipes has been studied by some authors. Thiyagarajan *et al.*[12], Bau *et al.*[13] and Difelice *et al.*[14] have assumed that heat losses may be calculated using a conduction model. Thermal convection in the porous medium around buried pipes has been taken into account in experimental and theoretical works by Schrock *et al.*[15], Fernandez *et al.*[16], Farouk *et al.*[17], Bau[28], Himasekhar *et al.*[19] and Fand *et al.*[20]. Another numerical and experimental investigation of the problem of natural convection associated with a cylindrical heat source embedded in a box has been performed by Himasekhar and Bau[21].

To our knowledge no investigations aimed at studying the transient natural convection of a corrugated plate embedded in an enclosed porous medium have been published. In this work, the problem of transient natural convection about a heated corrugated plate embedded in an enclosed porous medium, which can be applied to casting, is studied. Due to the fact that both the inertia and boundary (viscous) effects are important for a large Darcy number, the extended Brinkman–Forchheimer–Darcy equations are used for the momentum equations. A finite difference solution of the governing equations is obtained in terms of stream function, vorticity,

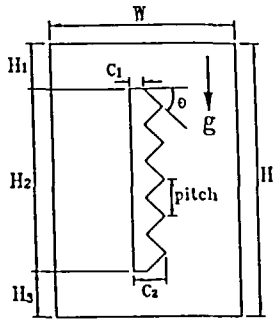

Figure 1 Physical model and coordinate

and temperature in a body-fitted coordinate system. The effects of Darcy number, Darcy–Rayleigh number, aspect ratio of the enclosure and plate position on the flow structure and heat transfer chacteristics are discussed. The results for a corrugated plate and a flat plate are compared. In addition, the numerical results obtained with four different models are also compared in order to investigate the inertia and boundary (viscous) effects.

MATHEMATICAL FORMULATION

Consider a corrugated plate of length H_2, thickness C_2, and corrugated angle θ embedded in an enclosed porous medium a shown in *Figure 1*. The corrugated plate is kept at a uniform temperature T_h^* while the wall temperature of the cavity is kept at room temperature T_c^* where $T_h^* > T_c^*$. For a mathematical formulation of the problem, it is assumed that (a) the fluid motion and temperature distribution in the porous medium are two-dimensional, (b) the fluid is incompressible, (c) frictional heating is negligible, (d) the thermophysical properties of the fluid are constant, (e) the Boussinesq approximation is applicable, (f) the porous medium is homogeneous and isotropic and (g) the fluid is in local thermal equilibrium with the porous matrix. With these assumptions, the governing equations for the conservation of mass, momentum and energy in cartesian coordinates for the problem of transient natural convection in a constant porosity medium are:

$$\frac{\partial u^*}{\partial x^*}+\frac{\partial v^*}{\partial y^*}=0 \tag{1}$$

$$\frac{\rho_f}{\varepsilon^2}\left(\varepsilon\frac{\partial u^*}{\partial t^*}+u^*\frac{\partial u^*}{\partial x^*}+v^*\frac{\partial u^*}{\partial y^*}\right)=-\frac{\partial p^*}{\partial x^*}-\frac{\mu_f}{K}u^*-\frac{\rho_f C}{\sqrt{K}}|w^*|u^*+\frac{\mu_f}{\varepsilon}\nabla^2 u^* \tag{2}$$

$$\frac{\rho_f}{\varepsilon^2}\left(\varepsilon\frac{\partial v^*}{\partial t^*}+u^*\frac{\partial v^*}{\partial x^*}+v^*\frac{\partial v^*}{\partial y^*}\right)=-\frac{\partial p^*}{\partial y^*}-\frac{\mu_f}{K}v^*-\frac{\rho_f C}{\sqrt{K}}|w^*|v^*+\frac{\mu_f}{\varepsilon}\nabla^2 v^*+\rho_f g\beta_f(T_h^*-T_c^*) \tag{3}$$

$$\sigma\frac{\partial T^*}{\partial t^*}+u^*\frac{\partial T^*}{\partial x^*}+v^*\frac{\partial T^*}{\partial y^*}=\alpha_e\nabla^2 T^* \tag{4}$$

where, u^* and v^* are the Darcian velocities in the x^* and y^* directions; w^* is the absolute velocity given by $w^*=(u^{*2}+v^{*2})^{1/2}$; p^* is the volumetric average pressure; ρ_f, μ_f, and β_f are the density, viscosity, and thermal expansion coefficient of the fluid; ε and K are the porosity and permeability of the porous medium which are assumed to be constant; g is the gravitational acceleration; $C=0.55$ is the Forchheimer coefficient[22]; α_e is the equivalent thermal diffusivity of

the saturated porous medium defined as $\alpha_e = k_e/\rho_f C_{p_f}$ with k_e denoting the stagnant thermal conductivity of the saturated porous medium; and $\sigma = [\varepsilon\rho_f C_{p_f} + (1-\varepsilon)\rho_s C_{p_s}]/(\rho_f C_{p_f})$ with C_{p_f} and C_{p_s} being the specific heats of the fluid phase and the solid phase at constant pressure.

We now introduce the following dimensionless variables:

$$x = \frac{x^*}{H_2}, \quad y = \frac{y^*}{H_2}, \quad u = \frac{u^* H_2}{\alpha_e}, \quad v^* = \frac{v^* H_2}{\alpha_e}, \quad w = \frac{w^* H_2}{\alpha_e}, \quad T = \frac{T^* - T_c^*}{T_h^* - T_c^*}, \quad t = \frac{\alpha_e t^*}{H_2^2} \tag{5}$$

where H_2 is the length of the plate. The resulting nondimensional equations for the stream function, vorticity, and temperature are given by:

$$\nabla^2 \Psi = -\Omega \tag{6}$$

$$\frac{1}{\varepsilon^2}(\varepsilon\Omega_t + \Psi_y\Omega_x - \Psi_x\Omega_y) = -\frac{Pr}{Da}\Omega + \frac{Pr}{\varepsilon}\nabla^2\Omega - \frac{C}{\sqrt{Da}}[(|w|v)_x - (|w|u)_y] + Ra\,Pr\,T_x \tag{7}$$

$$\sigma T_t + \Psi_y T_x - \Psi_x T_y = \nabla^2 T \tag{8}$$

where the dimensionless stream function and vorticity are defined as:

$$u = \frac{\partial \Psi}{\partial y}, \quad v = -\frac{\partial \Psi}{\partial x}, \quad \Omega = \frac{\partial v}{\partial x} - \frac{\partial u}{\partial y} \tag{9}$$

In (7) $Pr = \nu/\alpha_e$ is the Prandtl number, $Da = K/H_2^2$ is the Darcy number, $Ra = g\beta_f(T_h^* - T_c^*)H_2^3/\nu\alpha_e$ is the Rayleigh number.

Initially, the fluid in the porous medium is stationary and at a uniform temperature T_c^*. Thus, the dimensionless initial conditions are:

$$\Psi = \Omega = T = 0 \tag{10}$$

The dimensionless boundary conditions on the plate are:

$$\Psi = 0, \quad T = 1, \quad \Omega = -\Psi_{nn} \tag{11}$$

on the vertical walls of the cavity are:

$$\Psi = T = 0, \quad \Omega = -\Psi_{xx} \tag{12a}$$

and on the horizontal walls of the cavity are:

$$\Psi = T = 0, \quad \Omega = -\Psi_{yy} \tag{12b}$$

NUMERICAL PROCEDURES

The governing equations with the initial and boundary conditions in the cartesian coordinates (x,y) are transformed into the body-fitted coordinates (ξ,η). The method used to generate the grid is similar to that developed by Thomas and Middlecoff[23], in which the mesh is generated by solving a system of the form:

$$\xi_{xx} + \xi_{yy} = P(\xi,\eta) \tag{13}$$

$$\eta_{xx} + \eta_{yy} = Q(\xi,\eta) \tag{14}$$

with the boundary conditions specified in terms of the values of ξ and η on the boundaries. Since it is desirable to perform all numerical computations in the transformed plane, the dependent and independent variables in (13) and (14) must be interchanged according to the following transformations:

$$F_x = (y_\eta F_\xi - y_\xi F_\eta)/J \tag{15}$$

$$F_y=(x_\xi F_\eta - x_\eta F_\xi)/J \tag{16}$$

where F is any function. With the aid of (15) and (16), (13) and (14) become:

$$\alpha x_{\xi\xi} - 2\beta x_{\xi\eta} + \gamma x_{\eta\eta} + J^2(Px_\xi + Qx_\eta) = 0 \tag{17}$$

$$\alpha t_{\xi\xi} - 2\beta x_{\xi\eta} + \gamma y_{\eta\eta} + J^2(Py_\xi + Qy_\eta) = 0 \tag{18}$$

where α, β, and γ are the transformation coefficients and J is the Jacobian of the transformation given by:

$$\alpha = x_\eta^2 + y_\eta^2, \qquad \beta = x_\xi x_\eta + y_\xi y_\eta \tag{19a}$$

$$\gamma = x_\xi^2 + y_\xi^2, \qquad J = x_\xi y_\eta - x_\eta y_\xi \tag{19b}$$

The functions P and Q are coordinate control functions, which may be chosen so as to cause the coordinate lines to concentrate in certain parts of the domain. Here we take the combination of the functions developed by Thomas *et al.*[23] and Thompson *et al.*[24] as the control functions, i.e.:

$$P(\xi,\eta) = 0 \tag{20a}$$

$$Q(\xi,\eta) = [\psi(\xi,\eta) + \phi(\xi,\eta)](\eta_x^2 + \eta_y^2) \tag{20b}$$

where:

$$\phi(\xi,\eta) = -B\{sgn(\eta-\eta_{min})exp[-D(\eta-\eta_{min})] + sgn(\eta-\eta_{max})exp[-E(\eta_{max}-\eta)]\} \tag{21}$$

is discussed in Reference 24 and the function $\psi(\xi,\eta)$ is discussed in Reference 23. The boundary conditions for (17) and (18) are the values of the Cartesian coordinates x and y along the boundaries of the physical domain.

The equations (17) and (18) are discretized by the finite difference method over the transformed plane based on second order differencing, and the resulting nonlinear algebraic equations are solved numerically by the successive over-relaxation (SOR) technique. The numerical results would give the Cartesian coordinates (x,y) at discrete points (ξ,η) in the transformed domain.

After the transformation of governing equations (6)–(8) into the computational domain, one gets:

$$\tilde{\nabla}^2\Psi = -\Omega \tag{22}$$

$$\Omega_t + \frac{1}{\varepsilon J}(\Psi_\eta\Omega_\xi - \Psi_\xi\Omega_\eta) = -\frac{Pr\,\varepsilon}{Da}\Omega - \frac{C\varepsilon}{J\sqrt{Da}}[y_\eta(\tau_1)_\xi - y_\xi(\tau_1)_\eta - x_\xi(\tau_2)_\eta + x_\eta(\tau_2)_\xi]$$

$$+ Pr\,\tilde{\nabla}^2\Omega + \frac{Ra\,Pr\,\varepsilon}{J}(y_\eta T_\xi - y_\xi T_\eta) \tag{23}$$

$$T_t + \frac{1}{\sigma J}(\Psi_\eta T_\xi - \Psi_\xi T_\eta) = \frac{1}{\sigma}\tilde{\nabla}^2 T \tag{24}$$

where

$$\tau_1 = |w|v = [(x_\xi\Psi_\eta - x_\eta\Psi_\xi)^2 + (y_\xi\Psi_\eta - y_\eta\Psi_\xi)^2]^{1/2}(y_\xi\Psi_\eta - y_\eta\Psi_\xi)/J^2 \tag{25a}$$

$$\tau_2 = |w|u = [(x_\xi\Psi_\eta - x_\eta\Psi_\xi)^2 + (y_\xi\Psi_\eta - y_\eta\Psi_\xi)^2]^{1/2}(x_\xi\Psi_\eta - x_\eta\Psi_\xi)/J^2 \tag{25b}$$

The transformed initial conditions are:

$$\Psi(\xi,\eta,0) = \Omega(\xi,\eta,0) = T(\xi,\eta,0) = 0 \tag{26}$$

The transformed boundary conditions are:

$$\eta = \eta_{min}\text{: } \Psi = 0,\ T = 1,\ \Omega = -\gamma\Psi_{\eta\eta}/J^2 \tag{27a}$$

$$\eta = \eta_{max}\text{: } \Psi = 0,\ T = 0,\ \Omega = -\gamma\Psi_{\eta\eta}/J^2 \tag{27b}$$

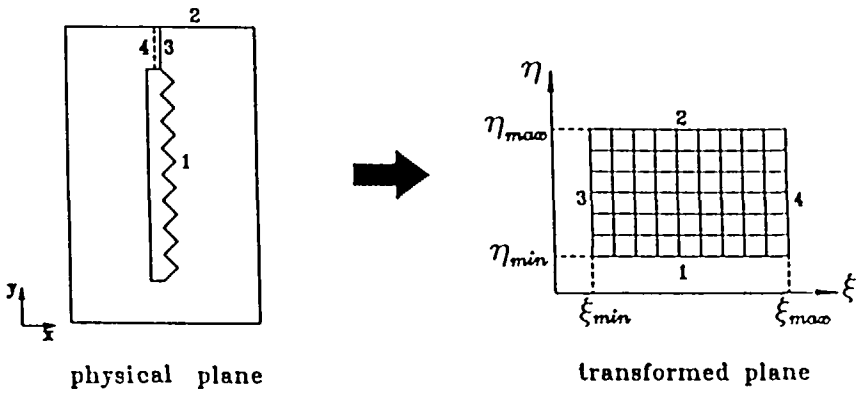

Figure 2 Coordinate transformation

where η_{max} and η_{min} are the outer and the inner boundaries in the transformed plane (*Figure 2*), respectively.

Equations (22)–(25) are discretized by the finite difference method based on central difference scheme. The finite difference equation for the stream function was solved by the successive over-relaxation method, while the finite difference equations for the vorticity and energy equation were solved by the alternative direction implicit (ADI) method. The necessary number of grid points depend on the Rayleigh number and the aspect ratio of the cavity. Trial calculations were necessary to check computation accuracy. A grid of 65×30 nodal points was found to be sufficiently accurate. A body-fitted curvilinear mesh system with 65×30 nodal points was shown in *Figure 3*. All computations were performed with a time increment of $\Delta t = 1.0 \times 10^{-4}$.

The convergence criterion for steady state solution was met when the relative difference in two consecutive time steps satisfied a prescribed tolerance given by:

$$\left|\frac{f^{m+1}-f^m}{f^{m+1}}\right| \leqslant 10^{-4} \tag{28}$$

where f stands for Ψ, Ω, and T while m is the number of iteration. After the convergence criteria had been satisfied, computations were carried out for the local and mean Nusselt numbers at the plate which are defined as:

$$Nu = -\frac{\partial T}{\partial n} = \left[\frac{1}{J\sqrt{\gamma}}(-\gamma T_\eta + \beta T_\xi)\right]_{\eta=\eta_{min}} \tag{29}$$

$$\overline{Nu} = \int_{\xi_{min}}^{\xi_{max}} Nu\,d\xi \Big/ \int_{\xi_{min}}^{\xi_{max}} d\xi \tag{30}$$

RESULTS AND DISCUSSION

The parameters shown in the governing equations (6)–(8) and boundary conditions (10)–(12) are C_2/H_2, H_3/H_2, W/H_2, H/H_2, corrugated pitch, corrugated angle θ, Ra, Pr, σ, ε and Da. A parameteric study was carried out for $C = 0.55$, $\varepsilon = 0.9$, $Pr = 0.7$, $C_2/H_2 = 1/8$, $\theta = 45°$, $H/H_2 = 5$, and pitch/$H_2 = 1/8$, with H_3/H_2 ranging from 1.5 to 2, W/H_2 from 2 to 5, Da from 10^{-4} to 10^{-1}, and Ra_m from 0 to 10^3.

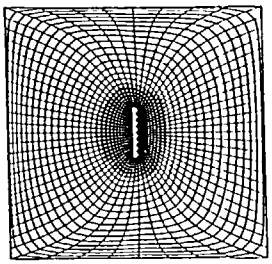

Figure 3 A typical example of the body-fitted coordinates

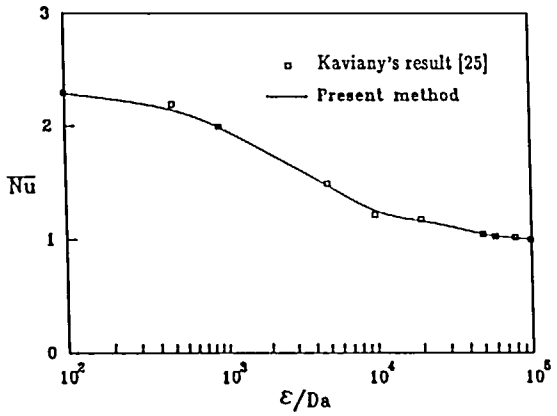

Figure 4 Steady state mean Nusselt number versus ε/Da for a concentric porous annulus with $T_h^* > T_c^*$ at $Ra = 10^6$, $R = 2$, $Pr = 0.05$, and $C = 0.5$

Accuracy of the numerical solution

Since no experimental or numerical solution to the problem of natural convection of a corrugated plate embedded in a porous medium has been reported in the literature, computations were first carried out for steady natural convection in a concentric porous annulus with $T_h^* > T_c^*$ corresponding to the case computed by Kaviany[25] for $R = 2$, $Ra = 10^6$, $Pr = 0.05$ and $C = 0.5$ to check the accuracy of the numerical solution. *Figure 4* shows that the Nusselt numbers (as a function of ε/Da) obtained in the present paper (solid line) are in good agreement with those obtained by Kaviany[25].

Steady state flow and heat transfer characteristics

The steady state flow and heat transfer characteristics of a corrugated plate embedded in a porous cavity are presented in *Figures 5–8*. *Figure 5* shows the steady isotherms (left) and streamlines (right) for a corrugated plate embedded in a porous cavity with $W/H_2 = H/H_2 = 5$, $C_2/H_2 = 1/8$, $H_1/H_2 = H_3/H_2 = 2$, pitch$/H_2 = 1/8$, $\theta = 45°$, $Pr = 0.7$, $\varepsilon = 0.9$ and $Da = 10^{-4}$. As shown in *Figure 5*(a) for $Ra_m = 30$, the heat transfer mechanism inside the cavity is conduction dominated, as evident from the weak circulation around the plate. The centres of the two counterrotating vortices are located slightly above the heated plate. The flow and temperature fields inside the cavity are almost symmetric with the vertical axis of the cavity.

As the Darcy–Rayleigh number is increased to 100 (*Figure 5b*), the plume clearly rises above the plate, and the centres of the vortices move upward with increasing strength. Due to the

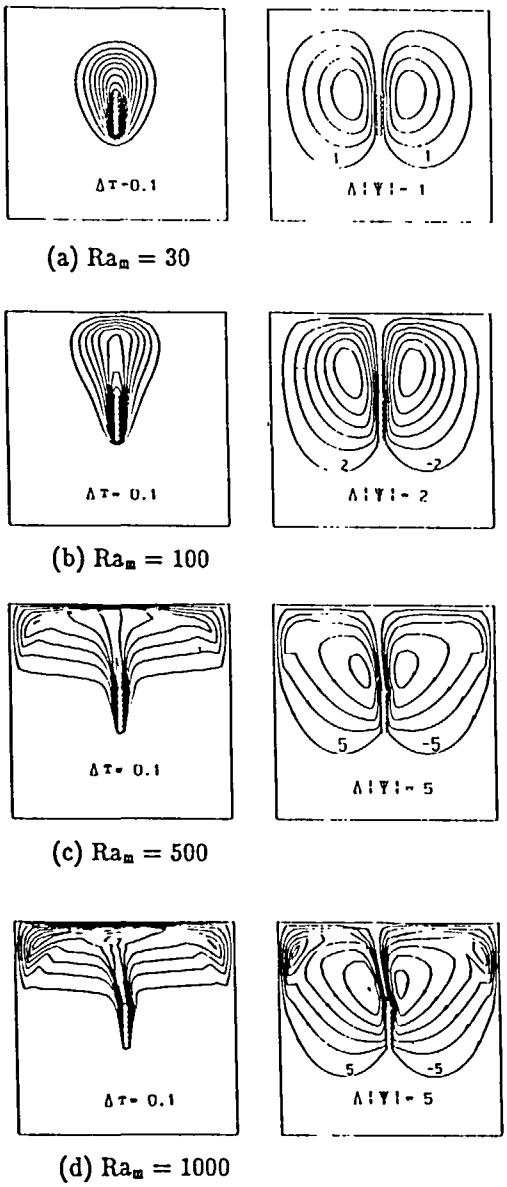

Figure 5 Steady state isotherms (left) and streamlines (right) for a corrugated plate embedded in a porous cavity with $W/H_2 = H/H_2 = 5$, $C_2/H_2 = 1/8$, $H_1/H_2 = H_3/H_2 = 2$, pitch/$H_2 = 1/8$, $\theta = 45°$, $Pr = 0.7$, $\varepsilon = 0.9m$, and $Da = 10^{-4}$ (a) $Ra_m = 30$, (b) $Ra_m = 100$, (c) $Ra_m = 500$, and (d) $Ra_m = 1000$

influence of the corrugated configuration, the flows on the right hand side of the plate are slightly slower than those on the left hand side. In this case, the flow pressure on the right portion of the cavity is larger than that on the left. As a result of the pressure difference, an extra horizontal driving force is created, which then acts on the fluid from right to left. As a result, the flow field is no longer symmetric with the vertical axis of the cavity.

With further increases in Ra_m to 500 (*Figure 5c*), the strength of the plume rising above the plate is increased and consequently increases in the velocity of the rising fluid. Due to the higher

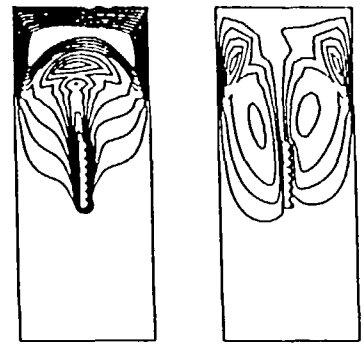

Figure 6 Steady state isotherms (left) and streamlines (right) for a corrugated plate with $W/H_2=2$, $H/H_2=5$, $C_2/H_2=1/8$, $H_1/H_2=H_3/H_2=2$, pitch/$H_2=1/8$, $\theta=45°$, $Pr=0.7$, $\varepsilon=0.9$, $Da=10^{-4}$, and $Ra_m=500$

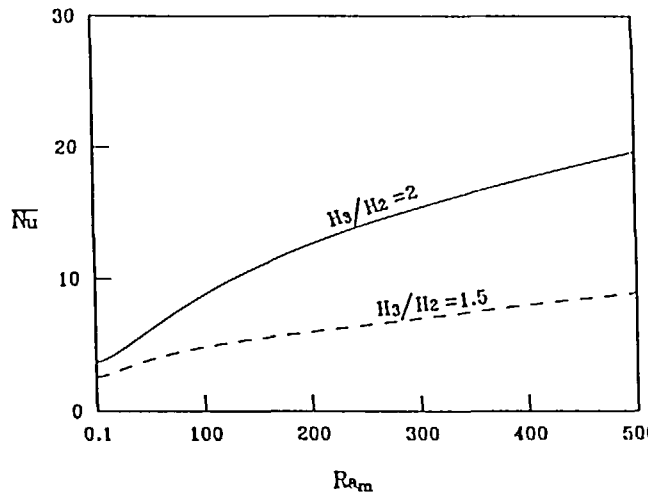

Figure 7 Effect of plate position on steady mean Nusselt number for a corrugated plate embedded in a porous cavity with $W/H_2=H/H_2=5$, $\theta=45°$, pitch/$H_2=1/8$, $C_2/H_2=1/8$, $Pr=0.7$, $\varepsilon=0.9$, and $Da=10^{-4}$

velocity, the thermal boundary layer which developed around the corrugated plate becomes thinner and the pressure difference between the right and left portion of the cavity is also increased. Thus, the distorsion of the streamlines and isotherms is more pronounced. When the Darcy-Rayleigh number is increased further to 1000 (*Figure 5d*), secondary vortices begin to appear at downstream of the heated plate in the upper corners of the porous cavity. This is due to the viscous effect associated with the high velocities of the upward fluids. These secondary vortices cause the instability in the porous cavity. *Figure 6* shows the isotherms (left) and streamlines (right) for a corrugated plate embedded in a porous cavity with the same parameters in the case of *Figure 5(d)* instead of the aspect ratio of the cavity (W/H) is reduced from 1 to 0.4 and Ra_m is reduced from 1000 to 500. In this figure, secondary vortices also appeared. Thus, it can be concluded that the value of Ra_m for appearing a secondary vortex is reduced for a smaller aspect ratio of the cavity (W/H). And the instability is increased with decrease in the aspect ratio of the cavity.

Figure 7 shows the effect of plate position on the steady mean Nusselt number for a corrugated plate. In this figure, the results are computed by varying the value of H_3/H_2 and keeping the

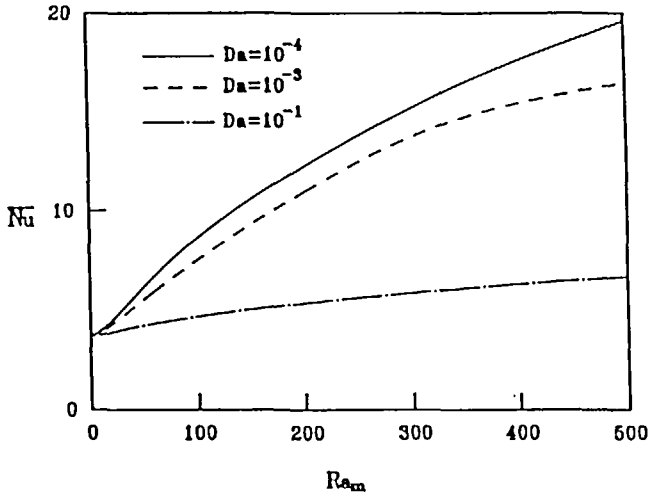

Figure 8 Effect of Darcy number on steady mean Nusselt number for a corrugated plate embedded in a porous cavity with $W/H_2=H/H_2=5$, $\theta=45°$, pitch/$H_2=1/8$, $C_2/H_2=1/8$, $Pr=0.7$, and $\varepsilon=0.9$

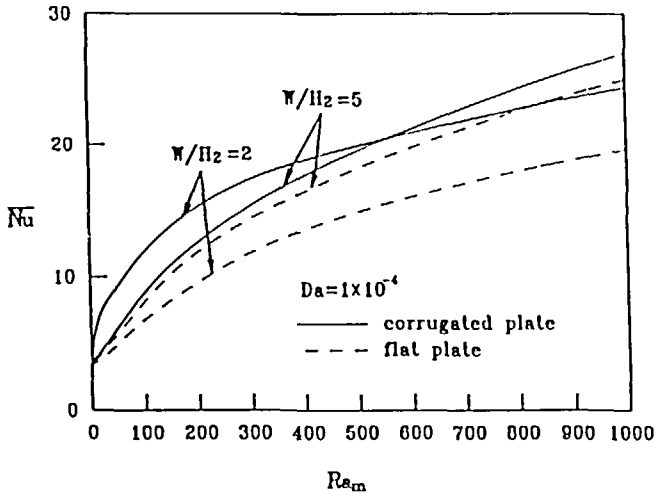

Figure 9 Effect of cavity aspect ratio on stady mean Nusselt number for $H/H_2=5$, $C_2/H_2=1/8$, $H_1/H_2=H_3/H_2=2$, $Pr=0.7$, $\varepsilon=0.9$ and $Da=10^{-4}$

other parameters with $W/H_2=H/H_2=5$. The results shown that $\overline{Nu}$ is decreased if the plate is moved downward along the vertical axis of the cavity.

The effects of Darcy number on the steady average Nusselt number as a function of the Darcy–Rayleigh number are shown in *Figure 8*. From this figure, it can be concluded that the steady mean Nusselt number increases with decreasing in Darcy number when the other parameters are fixed.

Figure 9 presents the effect of aspect ratio of the cavity on the steady mean Nusselt number for a corrugated plate and a flat plate embedded in a porous cavity. For a corrugated plate (solid lines), the steady mean Nusselt number increases as the aspect ratio is reduced when the

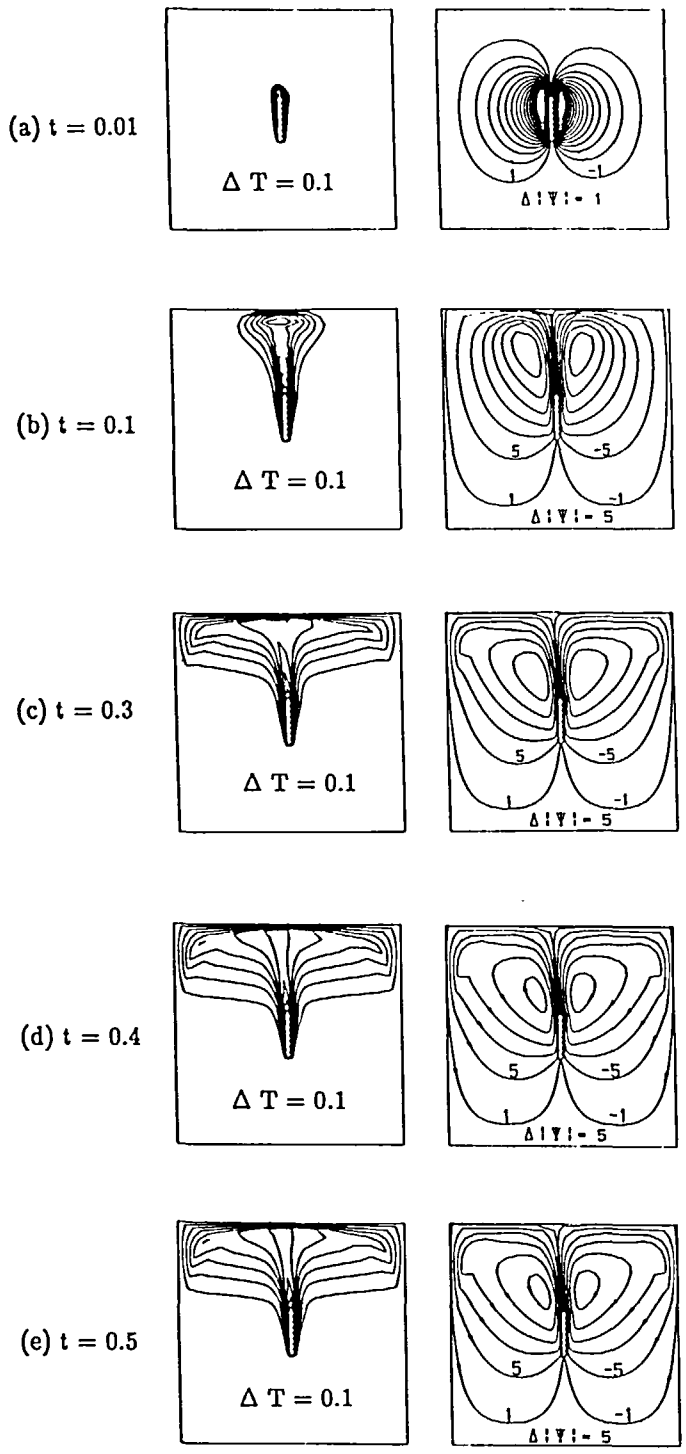

Figure 10 Transient isotherms (left) and streamlines (right) for $W/H_2 = H/H_2 = 5$, $C_2/H_2 = 1/8$, pitch/$H_2 = 1/8$, $\theta = 45°$, and $Ra_m = 500$, (a) $t = 0.01$, (b) $t = 0.1$, (c) $t = 0.3$, (d) $t = 0.4$, and (e) $t = 0.5$

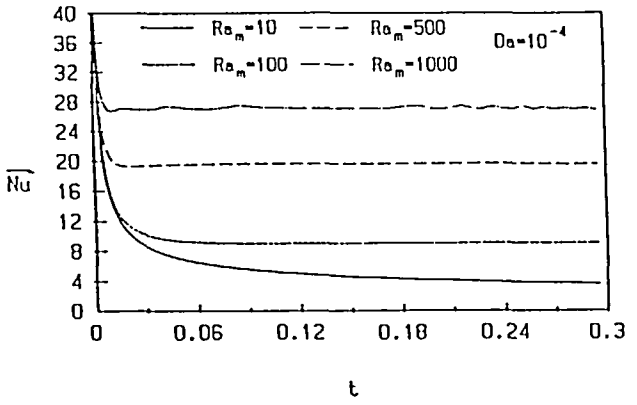

(a) Corrugated plate

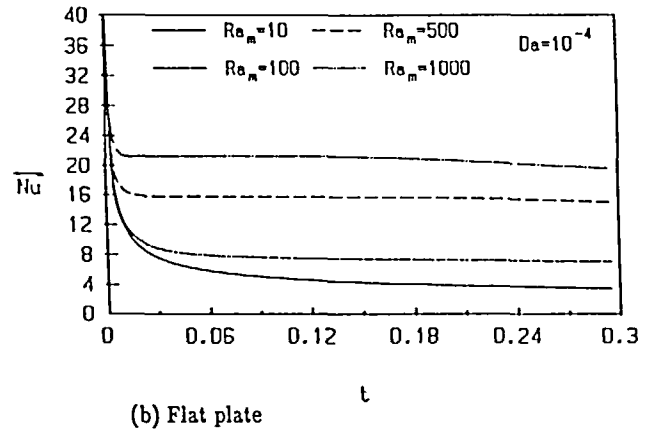

(b) Flat plate

Figure 11 Time history of the Nusselt number for $W/H_2 = H/H_2 = 5$, $C_2/H_2 = 1/8$, $H_1/H_2 = H_3/H_2 = 2$, $\sigma = 3$, $Pr = 0.7$, $\varepsilon = 0.9$, $Da = 10^{-4}$ and various Darcy-Rayleigh numbers, (a) corrugated plate ($\theta = 45°$, pitch/$H_2 = 1/8$), (b) flat plate

Darcy–Rayleigh number is less than 550, while there is an opposite effect as Darcy–Rayleigh number exceeds 550.

Transient characteristics

The numerical results for the transient flow and heat transfer characteristics are presented in *Figures 10* and *11*. *Figure 10* shows the time evolution of the flow and temperature fields for $Ra_m = 500$ at dimensionless time of $t = 0.01$, $t = 0.1$, $t = 0.3$, $t = 0.4$ and $t = 0.5$. The effect of the corrugated shape in vortices generation is clearly depicted in this figure. As the time progresses, the vortices move upward and transport the energy far away from the heated plate. Furthermore the steamlines and isotherms in *Figure 10(d)* ($t = 0.5$) are almost the same, indicating that the flow reaches the steady state at $t = 0.4$.

The transient behaviour of the mean Nusselt numbers for a corrugated plate with $W/H_2 = H/H_2 = 5$, $C_2/H_2 = 1/8$, $H_1/H_2 = H_3/H_2 = 2$, $\theta = 45°$, pitch/$H_2 = 1/8$, $\sigma = 3$, $Pr = 0.7$, $\varepsilon = 0.9$, and $Da = 10^{-4}$, at different Darcy–Rayleigh number are shown in *Figure 11(a)*. It is shown that the transient mean Nusselt number increases with increase in the Darcy–Rayleigh number. Initially, the sharp temperature gradients between the heat plate and porous medium are

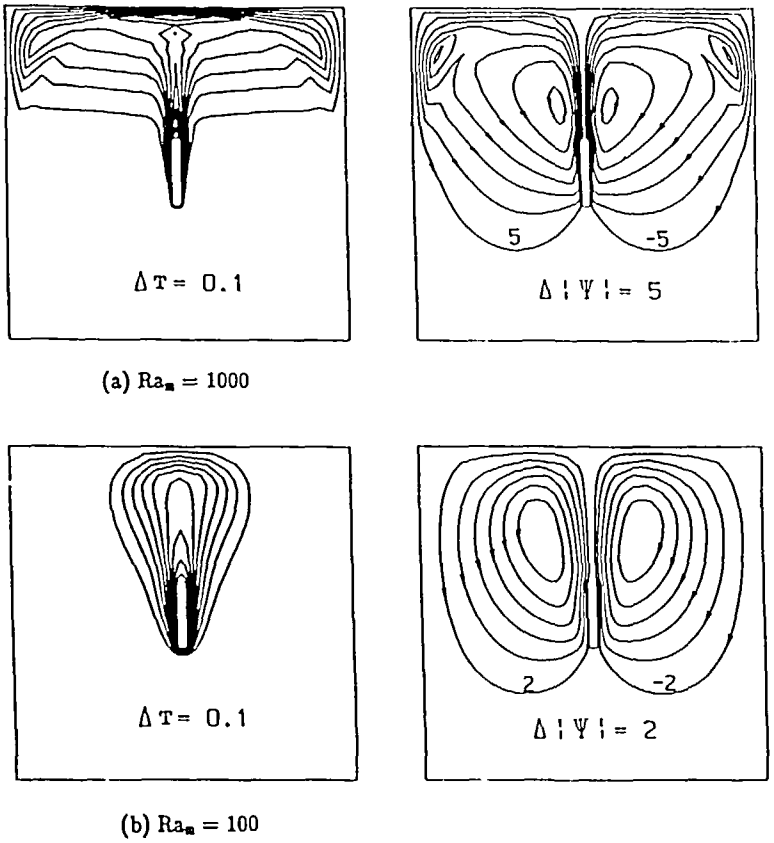

Figure 12 Steady state isotherms (left) and streamlines (right) for a flat plate embedded in a porous cavity with $W/H_2 = H/H_2 = 5$, $C_2/H_2 = 1/8$, $H_1/H_2 = H_3/H_2 = 2$, $Pr = 0.7$, $\varepsilon = 0.9$, and $Da = 10^{-4}$, (a) $Ra_m = 1000$, (b) $Ra_m = 100$

responsible for a rapid rate of heat transfer and their corresponding high Nusselt numbers. As shown in *Figure 11(a)*, for $Ra_m \leqslant 500$, the Nusselt number asymptotically approaches a steady state value. As Ra_m increases to 1000, the Nusselt number oscillates with a very small amplitude. The oscillation continues to $t = 0.09$ and then keeps at a stable value until $t = 0.18$. As time increases to $t > 0.18$, oscillation occurs again and the Nusselt number finally approaches a stable value. With further increases in Ra_m, the frequency of these oscillations increases and no stable solution can be obtained again.

COMPARISON OF A CORRUGATED PLATE WITH A FLAT PLATE

In order to see the corrugated configuration effect on the flow and heat transfer characteristics, computations were performed with $Pr = 0.7$, $\varepsilon = 0.9$, and plate aspect ratio $(C_2/H_2) = 1/8$ at various Darcy–Rayleigh numbers and cavity aspect ratios.

The computational results are presented in *Figure 9* and *Figures 11–13*. *Figure 9* shows the effect of the cavity aspect ratio on the steady mean Nusselt number for both a corrugated plate and a flat plate embedded in a porous cavity. As mentioned earlier, for $Ra_m < 550$, the steady mean Nusselt number for a corrugated plate is increased as the aspect ratio of the cavity (W/H) is reduced from 1 to 0.4 while keeping the value of H/H_2 at 5, and an opposite effect is obtained

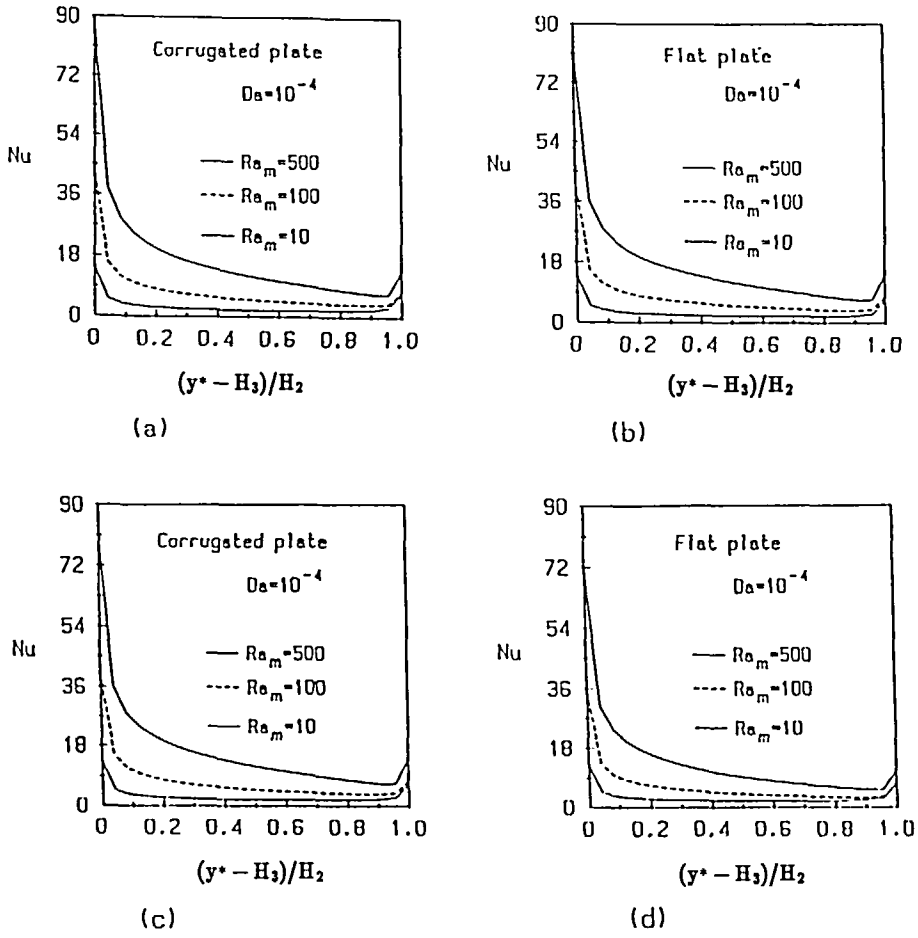

Figure 13 Variations of local Nusselt number at steady state condition with $H/H_2=5$, $C_2/H_2=1/8$, $H_1/H_2=H_3/H_2=2$, $Pr=0.7$, $\varepsilon=0.9$, and $Da=10^{-4}$, (a) corrugated plate ($W/H=1$), (b) flat plate ($W/H=1$), (c) corrugated plate ($W/H=2/5$), (d) flat plate ($W/H=2/5$)

as $Ra_m>550$. For a flat plate, however, the steady mean Nusselt number always decreases with decreasing in the value of W/H. This is due to the fact that the flow field is influenced by the corrugated configuration. *Figures 11(a)* and *11(b)* present the typical transient Nusselt numbers of the corrugated plate and flat plate respectively. The results are obtained with $W/H_2=H/H_2=5$, $C_2/H_2=1/8$, $H_1/H_2=H_3/H_2=2$, $\sigma=3$, $Pr=0.7$, $\varepsilon=0.9$, and $Da=10^{-4}$. It can be seen that, for both plates, the transient behaviour of the Nusselt number is very stable for $Ra_m<1000$. As Ra_m increases to 1000, the transient Nusselt number of a corrugated plate begins to oscillate with a small amplitude as previously discussed, while that of a flat plate keeps in stable.

Figures 12(a) and *(b)* show the isotherms (left) and streamlines (right) for a flat plate embedded in a porous cavity with $W/H_2=H/H_2=5$, $C_2/H_2=1/8$, $H_1/H_2=H_3/H_2=2$, $Pr=0.7$, $\varepsilon=0.9$, and $Da=10^{-4}$ at $Ra_m=1000$ and 100, respectively. Comparing them with *Figure 5*, one can see that the isotherms and streamlines, for a flat plate, are always symmetric with respect to the vertical axis of the cavity, while those for a corrugated plate are not symmetric with this vertical axis.

The variations of the steady local Nusselt numbers on the flat surface (left surface) of a corrugated plate with $Da=10^{-4}$, $\varepsilon=0.9$, and $Pr=0.7$, at $Ra_m=10$, 100 and 500 for

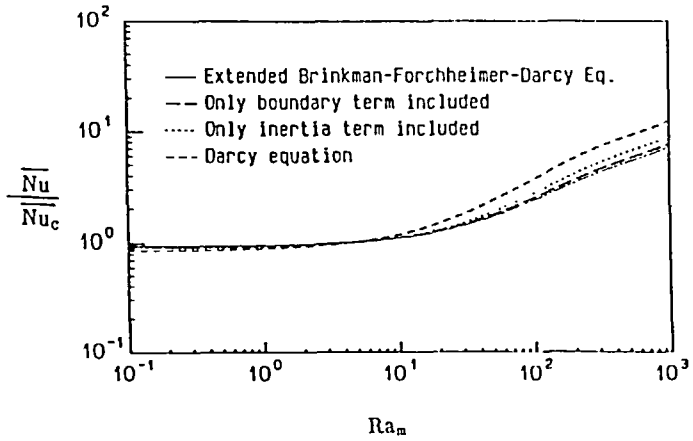

Figure 14 Effect of inertia and boundary terms on $\overline{Nu}/\overline{Nu_c}$ for a corrugated plate with $W/H_2 = H/H_2 = 5$, $C_2/H_2 = 1/8$, $H_1/H_2 = H_3/H_2 = 2$, $Pr = 0.7$, $\varepsilon = 0.9$, and $Da = 10^{-4}$ at various Ra_m

$W/H_2 = H/H_2 = 5$ and $W/H_2 = H/H_2 = 2$ are presented in *Figures 13(a)* and *13(c)*, respectively. The results show that the local Nusselt number increases with increase in Darcy–Rayleigh number. Comparing these two figures, we see that the local Nusselt number decreases with decreasing in aspect ratio of the cavity. The discrepancy is more pronounced at a larger Ra_m. The computational results for a flat plate with the same parameters are shown in *Figures 13(b)* and *13(d)*. *Figure 13(b)* shows the steady local Nusselt number on the left surface for a flat plate with $W/H = 1$ while *Figure 13(d)* shows the results for a flat plate with $W/H = 2/5$. It shows that the variation tendency of the steady local Nusselt number for both a corrugated and a flat plate is the same. The results show that, the local Nusselt number, for both plates, has a maximum value at the stagnation point (lower left corner of the plate) then decreases monotonously along the plate surface to the position leading to the top of the plate and with a slight increase at the separation point. Comparing the four figures in *Figure 13*, it shows that the local Nusselt numbers of a corrugated plate are greater than those for a flat plate. These figures also show that the local Nusselt number increases with increase in Darcy–Rayleigh number.

Effects of inertia and boundary (viscous) terms

Figure 14 shows the inertia and boundary (viscous) effects on $\overline{Nu}/\overline{Nu_c}$ (where $\overline{Nu_c}$ is the Nusselt number for heat conduction) for a corrugated plate with $W/H_2 = H/H_2 = 5$, $\theta = 45°$, pitch/$H_2 = 1/8$, $C_2/H_2 = 1/8$, $Pr = 0.7$, and $\varepsilon = 0.9$ at different values of Ra_m. The results are obtained based on four different models, including the pure Darcy, Brinkman–Darcy, Forchheimer–Darcy, and Brinkman–Forchheimer–Darcy equations. As indicated in the figure, the Nusselt number is the highest for the model with Darcy's law while the Nusselt number is smallest for the model with extended Brinkman–Forchheimer–Darcy equation. Note that the curves begin to deviate from unity between $Ra_m = 20$ and 30 depending on the particular model used. These are the critical Rayleigh numbers for the onset of free convection for a corrugated plate in a porous cavity. From this figure, it can be concluded that both the inertia and boundary effects tend to reduce the heat transfer rate, but the effect of inertia term is more prominent than that of boundary term. Both the inertia and boundary effects are significant after the free convection is predominant, and should be considered simultaneously at a large Darcy–Rayleigh number.

CONCLUDING REMARKS

The problem of non-Darcian transient natural convection for a corrugated plate embedded in an enclosed porous medium is studied numerically. The extended Brinkman–Forchheimer–Darcy equations were used as the governing equations and were solved the body-fitted coordinates by the finite difference method. The following conclusions can be drawn fron the present study:

1 For a corrugated plate, the flow and temperature fields are almost symmetric with the vertical axis of the enclosure as the heat transfer is dominated by conduction mode, and the flow fields are no longer symmetric with respect to this vertical axis after the onset of free convection. The discrepancy increases with increase in Ra_m.
2 For a corrugated plate, the transient Nusselt number begins to oscillate with a very small amplitude as Ra_m is increased to 1000. With further increase in Ra_m, the frequency of oscillation increases and no stable solution can be obtained.
3 The heat transfer rate is decreased as the plate position is changed downward along the vertical axis of the enclosure.
4 For a fixed Ra_m and aspect ratio of the cavity, the overall heat transfer rate is increased as Darcy number is decreased.
5 The steady mean Nusselt number for a corrugated plate increases with decreasing in the aspect ratio of the cavity as the Darcy–Rayleigh number is less than a critical value (550), and the opposite result is obtained as the Darcy–Rayleigh number is greater than this critical value. The steady Nusselt number for a flat plate, however, increases with the aspect ratio of the cavity at all values of Ra_m.
6 The local Nusselt number has a maximum value at the stagnation point, and decreases monotonously to the position near the separation point.
7 Steady state is reached at a dimensionless time of $t=0.4$ for $\sigma=3$.
8 The overall heat transfer rate for a corrugated plate, for fixed parameters, is greater than that for a flat plate.
9 The value of Ra_m for beginning to appear a secondary vortex for a corrugated plate embedded in a porous cavity decreases with decrease in aspect ratio of the cavity.
10 Both the inertia and boundary (viscous) terms have the effect of reducing the heat transfer rate and are significant after the free convection is predominant.

REFERENCES

1 Walker, K. L. and Homsey, G. M. Convection in a porous cavity, *J. of Fluid Mechanics*, **87**, 449–474 (1978)
2 Prasad, V. and Kulacki, F. A. Natural convection in a rectangular porous cavity with constant heat flux on one vertical wall, *J. Heat Transfer*, **106**, 152–157
3 Prasad, V. and Kulacki, F. A. Convective heat transfer in a rectangular porous cavity—effect of aspect ratio on flow structure and heat transfer, *J. Heat Transfer*, **106**, 158–165 (1984)
4 Tong, T. W. and Subramanian, E. A boundary layer analysis for natural convection in vertical porous enclosures—use of the Brinkman-extended Darcy model, *Int. J. Heat Mass Transfer*, **28**, 563–571 (1985)
5 Beckermann, C., Viskanta, R. and Ramadhyani, S. A numerical study of non-Darcian natural convection in a vertical enclosure filled with a porous medium, *Num. Heat Transfer*, **10**, 557–570 (1986)
6 Beckermann, C., Ramadhyani, S. and Viskanta, R. Natural convection flow and heat transfer between a fluid layer and a porous layer inside a rectangular enclosure, *J. Heat Transfer*, **109**, 363–370 (1987)
7 Georgiadis, J. and Catton, I. Prandtl number effect on Benard convection in porous media, *J. Heat Transfer*, **108**, 284–290 (1986)
8 Seki, N., Fukusako, S. and Inaba, H. Transfer in a confined rectangular cavity packed with porous media, *Int. J. Heat Mass Transfer*, **21**, 985–989 (1978)
9 Jonsson, T. and Catton, I. Prandtl number dependence of natural convection in porous media, *J. Heat Transfer*, **109**, 371–377 (1987)
10 Bejan, A. and Anderson, R. Heat transfer across a vertical impermeable partition imbedded in porous medium, *Int. J. Heat Mass Transfer*, **24**, 1237–1245 (1981)
11 Bejan, A. Natural convection heat transfer in a porous layer with internal flow obstructions, *Int. J. Heat Mass Transfer*, **26**, 815–822 (1983)

12 Thiyagarajan, R. and Yovanovich, M. M. Thermal resistance of buried cylinder with constant flux boundary condition, *J. Heat Transfer*, **96**, 249–250 (1974)
13 Bau, H. H. and Sadhal, S. S. Heat losses from a fluid flowing in a buried pipe, *Int. J. Heat Mass Transfer*, **25**, 1621–1629 (1982)
14 Difelice, R. F. and Bau, H. H. Conductive heat transfer between eccentric cylinders with boundary conditions of the third kind, *J. Heat Transfer*, **105**, 678–680 (1983)
15 Schrock, V. E., Fernandez, R. T. and Kesavan, K. Heat transfer from cylinders embedded in a liquid filled porous medium, *Proc. Int. Heat Transfer Conf.*, Paris, **VoL. VII**, Ct.3.6 (1970)
16 Fernandez, R. T. and Schrock, V. E. Natural convection around a heated cylinder buried in a saturated porous medium, *Proc. Int. Heat Transfer Conf.* Munich, **2**, 335–340 (1982)
17 Farouk, B. and Shayer, H. Natural convection around a heated cylinder buried in a saturated porous medium, *Proc. of the 23rd National Heat Transfer Conf.* Denver (1985)
18 Bau, H. H. Convective heat losses from a pipe buried in a semi-infinite porous medium, *Int. J. Heat Mass Transfer*, **27**, 2047–2056 (1984)
19 Himasekhar, K. and Bau, H. H. Thermal convective associated with hot/cold pipes buried in a semi-infinite saturated porous medium, *Int. J Heat Mass Transfer*, **30**, 263–273 (1987)
20 Fand, R. M., Steinbetger, T. E. and Cheng, P. Natural convection heat transfer from a horizontal cylinder embedded in a porous medium, *Int. J. Heat Mass Transfer*, **29**, 119–134 (1986)
21 Himasekhar, K. and Bau, H. H. Thermal convection around a heat source embedded in a box containing a saturated porous medium, *J. Heat Transfer*, **110**, 649–654 (1988)
22 Cheng, P. Heat transfer in geothermal systems, *Advances in Heat Transfer*, **14**, 1–105 (1978)
23 Thomas, P. D. and Middlecoff, J. F. Direct control of the grid point distribution in meshes generated by elliptic equations, *AIAA J.*, **18**, 652–656 (1980)
24 Thompson, J. F., Thames, F. C. and Mastin, C. W. TOMCAT—a code for numerical generation of boundary fitted curvilinear coordinate systems of fields containing any number of arbitrary two-dimensional bodies, *J. Comput. Phys.*, **24**, 274–302 (1977)
25 Kaviany, M. Non-Darcian effects on natural convection in porous media confined between horizontal cylinders, *Int. J. Heat Mass Transfer*, **29**, 1513–1519 (1986)